crystals

MDPI

Article

Simulation and Analysis of Microring Electric Field Sensor Based on a Lithium Niobate-on-Insulator

Zhenlin Wu [1], Yumeng Lin [1], Shaoshuai Han [1], Xiong Yin [1], Menghan Ding [1], Lei Guo [2], Xin Yang [3] and Mingshan Zhao [1,*]

[1] School of Optoelectronic Engineering and Instrumentation Science, Dalian University of Technology, Dalian 116024, China; zhenlinwu@dlut.edu.cn (Z.W.); xiaomengzi@mail.dlut.edu.cn (Y.L.); 779102711@mail.dlut.edu.cn (S.H.); yinxiong123@mail.dlut.edu.cn (X.Y.); dingmenghan@mail.dlut.edu.cn (M.D.)
[2] School of Information and Communication Engineering, Dalian University of Technology, Dalian 116024, China; leiguo@dlut.edu.cn
[3] Department of Electrical and Electronics Engineering, School of Engineering, Cardiff University, Cardiff CF10 3AT, UK; yangx26@cardiff.ac.uk
* Correspondence: mszhao@dlut.edu.cn; Tel.: +86-138-8960-3037

Abstract: With the increasing sensitivity and accuracy of contemporary high-performance electronic information systems to electromagnetic energy, they are also very vulnerable to be damaged by high-energy electromagnetic fields. In this work, an all-dielectric electromagnetic field sensor is proposed based on a microring resonator structure. The sensor is designed to work at 35 GHz RF field using a lithium niobate-on-insulator (LNOI) material system. The 2.5-D variational finite difference time domain (varFDTD) and finite difference eigenmode (FDE) methods are utilized to analyze the single-mode condition, bending loss, as well as the transmission loss to achieve optimized waveguide dimensions. In order to obtain higher sensitivity, the quality factor (Q-factor) of the microring resonator is optimized to be 10^6 with the total ring circumference of 3766.59 μm. The lithium niobate layer is adopted in z-cut direction to utilize TM mode in the proposed all-dielectric electric field sensor, and with the help of the periodically poled lithium niobate (PPLN) technology, the electro-optic (EO) tunability of the device is enhanced to 48 pm·μm/V.

Keywords: LNOI; microring resonator; electro-optical; PPLN

Citation: Wu, Z.; Lin, Y.; Han, S.; Yin, X.; Ding, M.; Guo, L.; Yang, X.; Zhao, M. Simulation and Analysis of Microring Electric Field Sensor Based on a Lithium Niobate-on-Insulator. *Crystals* **2021**, *11*, 359. https://doi.org/10.3390/cryst11040359

Academic Editor: Marco Bazzan

Received: 3 March 2021
Accepted: 26 March 2021
Published: 30 March 2021

1. Introduction

As a key component of modern photonic integrated circuits, microring resonator (MRR) shows great performance in filtering [1,2], sensing [3–6], ultra-fast electro-optic modulation (EOM) [7–10], optical frequency comb generation [11,12] and wavelength division multiplexing [13] due to its unique characteristics such as wavelength selection, compact structure and high quality factor (Q-factor). In the past decades, various material systems of MRR structures have been investigated for opto-electric applications, including graphene [14,15], silicon (Si) [16–18], indium phosphide (InP) [19], polymer [20] and lithium niobate [8,10,21]. Among these materials, Si and InP structures rely on plasma dispersion effect and quantum-confined Stark effect, respectively, which are not suitable for ultra-high-speed data transmission purposes. For graphene, the technical difficulty lies in the separation of monolayer structure and limitation for mass production [15], which makes it hard for commercialization. In addition, although the EO polymer has high EO coefficient, the thermal instability might cause the material decrease gradually with time. Lithium niobate ($LiNbO_3$, LN) is a synthetic material with excellent electro-optic, acoustic-optic, nonlinear-optic properties and good transmittance in the near-infrared band [22]. Lithium niobate-on-insulator (LNOI) has been developed as the platform for a variety of waveguide structures, such as LN waveguide [8,23,24], proton-exchange waveguide [25] and strip-loaded waveguide [26]. Due to the high electro-optic coefficient (γ_{33} = 31 pm/V)

and large refractive index (n_e = 2.138 and n_o = 2.21 at 1550 nm), lithium niobate-based EOM devices have been developed rapidly in recent years. In addition, several hybrid waveguide modulators have been proposed, such as Si-$LiNbO_3$ [9], Si_3N_4-$LiNbO_3$ [27]. However, as the RI of Si-Si_3N_4 is higher than or close to LN, the proportion of optical modes in LN will be decreased, reducing the interaction between electric and optical field, lowering the overall EO modulation efficiency of the device. In order to fabricate LN structure directly from the thin film, a series of work has been carried out to process this hard-to-etch material, and to date, ultra-low-loss $LiNbO_3$ waveguide has been proved to be as low as 2.7 dB/m [24,28].

With the miniaturization of electronic devices, the maximum voltage they can withstand is constantly reduced, which makes them very vulnerable to damage by high electromagnetic energy; therefore, several all-dielectric receivers based on bulk LN crystals have been investigated [29,30]. They use all dielectric antenna to receive the RF electric field in space, and then amplify by dielectric resonant antenna (DRA) resonance and utilize a LN disc resonator to modulate the optical field. However, this bulk structure is not conducive for integration. Another all-dielectric microring electric field sensor device proposed by Chen et al. using Si_3N_4-$LiNbO_3$ heterostructure has shown the ability for the detection of electric field of 1.86 GHz [3]. However, due to the small proportion of light which can propagate in the LN layer, it will lead to a lower EO overlap factor, giving rise to lower sensitivity of the device.

In this paper, LNOI structure is used as an EO platform to analyze the single-mode conditions, transmission loss, optical power distribution in LN, cladding thickness and finally determine the waveguide size, so that it has high EO overlap factor and low transmission loss. After strict theoretical calculation and software simulation, the design of microring electric field sensor which works at 35 GHz can be achieved. In order to avoid the phenomenon that net modulation is zero, a traditional receiving front end adopts the method of adjusting the distribution of resonant electrodes [31]. There are also proposed electrode-free front-ends to avoid zero modulation by exposing half of the receiving unit to the electric field [29,30]. However, neither of these two methods makes full use of the electro-optical performance of the RF receiving unit. Unlike any traditional methods, PPLN technology is introduced in this design. It makes full use of the electro-optical characteristics of the entire microring and improves the electro-optical tuneability to 48 pm·μm/V. Compared with the traditional electro-optic modulator with electrodes, the designed microring sensor does not involve any metal structure, which is able to avoid serious damages caused by external high-energy electromagnetic field.

2. Structure

The structure of the proposed device is illustrated in Figure 1. In this design, Si is used as the bottom substrate with a 2 μm thick SiO_2 layer on top as the lower cladding. A layer of z-cut lithium niobate film is selected as the core layer of the waveguide whose refractive index can vary with applied electric field. A layer of SiO_2 is covered on top of the whole device as a protection layer. The resonator is designed as an add-drop structure, the light satisfying the resonance condition oscillates continuously in the ring and interacting with the external electric field, thus realizing the efficient electro-optical modulation.

The variational finite difference time domain (varFDTD) method as a new solution for solving complex Maxwell equations can efficiently model microring resonators and have better time efficiency compared with 3-D FDTD. Finite difference eigenmode (FDE) is considered to be the most effective way to analyze mode distribution and calculate bending loss. In both cases, rectangular Cartesian grids are used to divide the waveguide geometry, and perfectly matched layer (PML) is used as the boundary condition. In order to ensure the accuracy of the results, the grid density is increased in the region with large refractive index change.

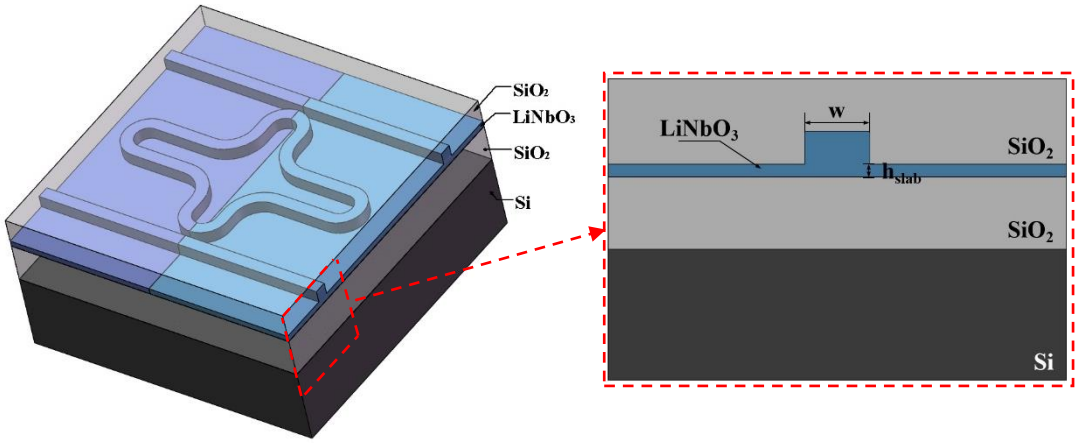

Figure 1. A schematic of periodically poled lithium niobate (PPLN) microring resonator (MRR) structure (blue and purple areas represent lithium niobate films with opposite polarization direction). Inset: schematic of cross-section of the waveguide structure, where w is the width of the waveguide and h_{slab} is the thickness of the residual layer.

3. Results and Discussion

In this work, a 1550 nm laser is adopted as carrier wave. At this wavelength, the extraordinary and ordinary refractive indices of LN are n_e = 2.138 and n_o = 2.211 [32], respectively, and the refractive index of SiO_2 is 1.444. The waveguide structure has a strong restriction on light energy due to the high-refractive-index difference (>0.7) of LNOI. The parameters of 600 nm LNOI film, which is used as the basic platform for the design, comes from NANOLN company (Jinan, China). To ensure that the signal will not decay due to modal dispersion, the single-mode condition in the waveguide should be satisfied. Firstly, the effect of the LN slab thickness on the effective refractive index n_{eff} is calculated, as shown in Figure 2a. With $h_{TE\text{-}slab} < 0.5$ μm and $h_{TM\text{-}slab} < 0.6$ μm, the transverse electric (TE) and transverse magnetic (TM) modes can be realized in the vertical direction for single-mode transmission, respectively. Figure 2b shows the bending loss corresponding to different LN slab thickness with fixed 0.8 μm waveguide width and 100 μm bending radius. It can be found that the reduction in the thickness of the slab area can lead to enhanced waveguide mode confinement and reduced bending loss; however, at the same time it can also cause difficulty in coupling between waveguides. In order to obtain the same coupling efficiency, the coupling distance gap is usually small, which requires complex fabrication procedures for the etching of the LN films. Figure 2c shows the results of the previous analysis, where it can be found that the coupling efficiency gradually descends with decreasing h_{slab}. By considering both the low-loss transmission in the waveguide and the effective coupling between waveguides, a thickness of 0.22 μm of the slab area of LN layer is eventually chosen to achieve better optical carrier transmission characteristics.

The thickness of the LN slab area is fixed at 0.22 μm, and the dependence of the effective refractive index on the ridge waveguide width w is shown in Figure 3a. The effective refractive index increases with increasing width of the waveguide, generating higher-order of waveguide modes. For TE and TM, the single-mode and multi-mode critical values appear near w = 1.1 μm and 0.9 μm, respectively. Therefore, it is necessary to select w smaller than the critical value to satisfy the single-mode condition. At the same time, since the transmission loss and the optical power in the lithium niobate showed a positive trend with the increase of w, it is necessary to choose a larger w so that the waveguide has low transmission loss and high mode confinement, as shown in Figure 3b. The higher the ratio of optical power in lithium niobate P_{LN} is, the larger the photo-electric overlap factor is, resulting in the greater electro-optical modulation efficiency of the device [26], as shown in Figure 3c. By weighing the relationship between the parameters, the waveguide width is determined to be 0.8 μm, and more than 80% of optical power is confined in LN waveguide area. Therefore, the TE and TM optical mode-field profile of the finally

designed $LiNbO_3$ ridge waveguide are obtained as shown in Figure 3d. It can be seen that this structure has good capability of modal constraint. For z-cut LN film, TE and TM mode accesses electro-optic coefficients γ_{13} = 8 pm/V and γ_{33} = 31 pm/V, respectively [33], so we choose 1550 nm TM polarized light as the carrier. In this case, the effective refractive index n_{eff} = 1.78596, group refractive index n_g = 2.27407, transmission loss can be calculated as 1.06670×10^{-5} dB/cm, and the optical power in lithium niobate P_{LN} = 81%.

In order to prevent external dust, humidity and other pollutants from changing the effective refractive index of the waveguide and thus affecting the performance of the microring, an upper cladding layer of SiO_2 is adopted on top of the LN film as the protection layer to increase the stability of the device. The effect of SiO_2 thickness on the effective refractive index is also simulated, as shown in Figure 4. When the SiO_2 thickness is more than 1 μm, n_{eff} tends to be stable, therefore, the thickness of SiO_2 protection layer is set to be 3 μm.

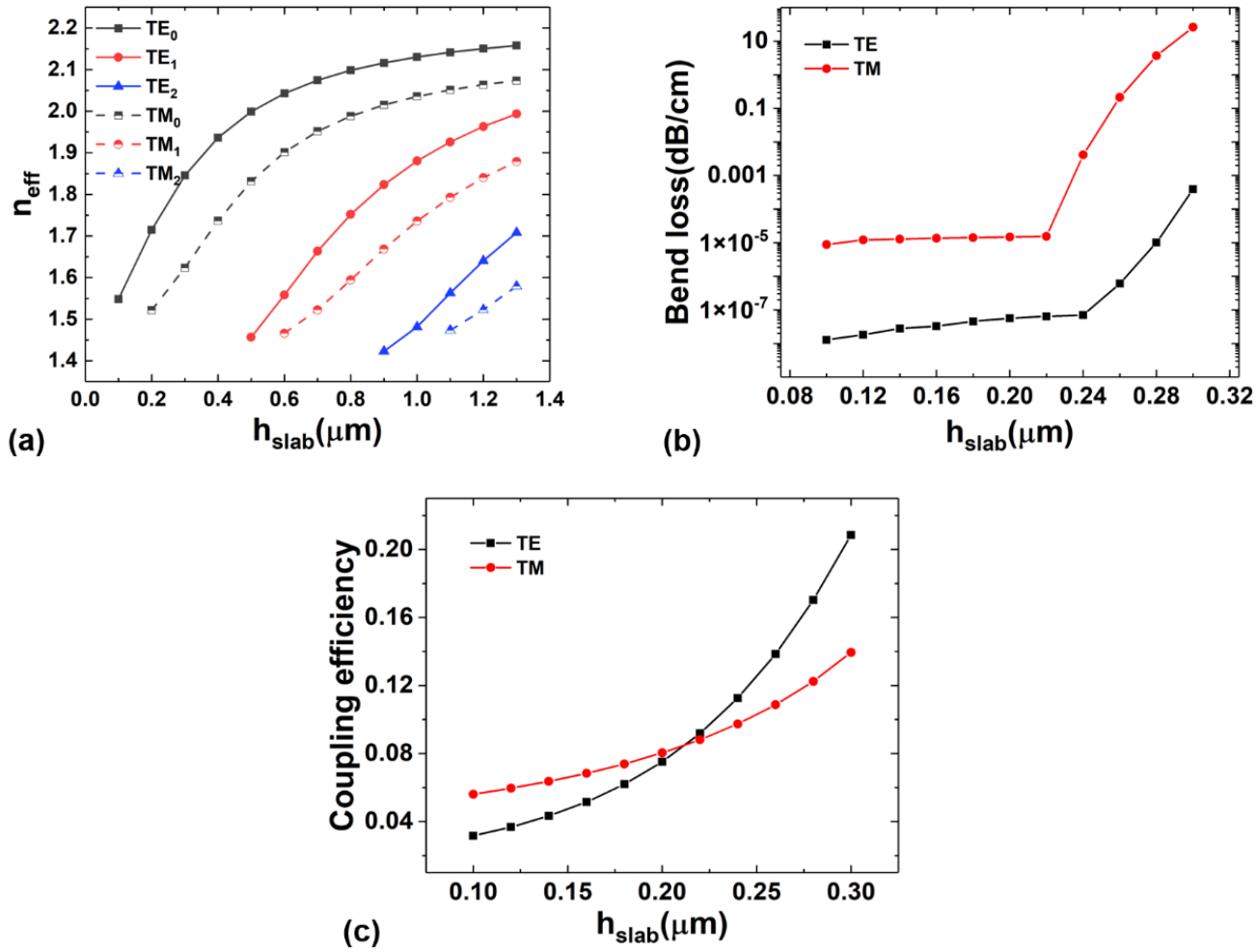

Figure 2. (**a**) Relationship between effective refractive index of lithium niobate-on-insulator (LNOI) slab waveguide with 1 μm upper cladding thickness and slab thickness. (**b**) The influence of the thickness of LN slab layer on bending loss with the waveguide width of 0.8 μm and the bending radius of 100 μm. (**c**) The dependence of the coupling efficiency and the thickness of the lithium niobate (LN) slab layer with coupling distance gap = 0.5 μm.

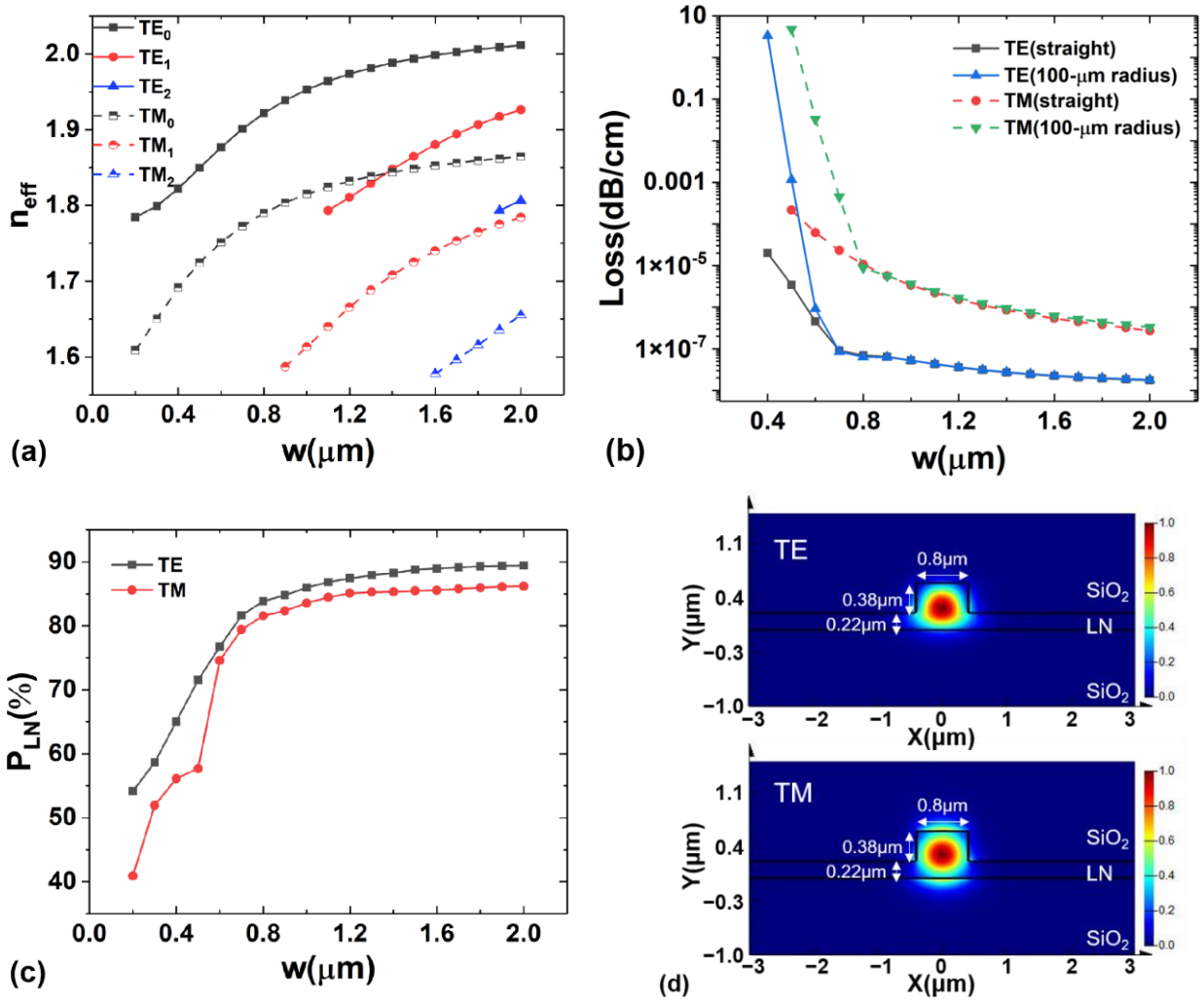

Figure 3. Dependence of (**a**) effective refractive index (**b**) transmission loss of straight waveguide/100 μm radius curved waveguide and (**c**) optical power ratio in lithium niobate on waveguide width. (**d**) Simulated transverse electric (TE) and transverse magnetic™ optical mode-field profile of a $LiNbO_3$ ridge waveguide with 0.22 μm thickness of slab layer and 0.8 μm width of waveguide at 1550 nm. Material boundaries are indicated by the black solid lines.

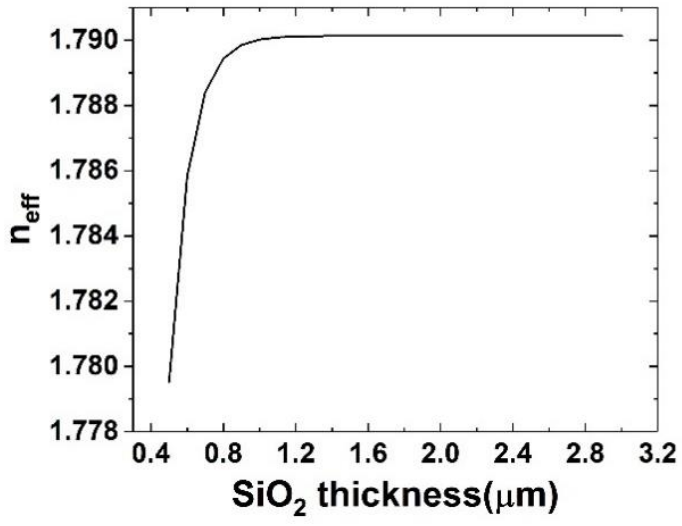

Figure 4. Relationship between the SiO_2 thickness and the effective refractive index.

As the radio frequency field is incident on the LNOI microring resonator, the output light intensity will change with the RF field intensity, as shown in Figure 5a. For better detection sensitivity, the input light needs to be set at the maximum slope of the resonance peak, so that even if the received RF signal is very weak, the modulated light intensity can still have a large variation. Figure 5b shows that when $f_{RF} = f_{FSR}$, RF modulation can be achieved as long as the modulation sidebands are located in the adjacent resonances.

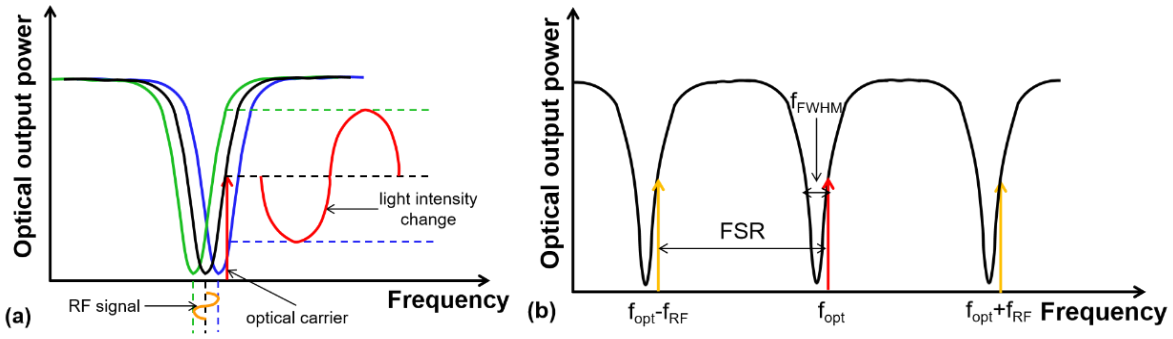

Figure 5. (**a**) Intensity modulation of microring resonator. The periodic change of RF signal (yellow line) causes the left and right drift of the microring transmission spectral line, which eventually leads to the periodic change of the intensity of the output laser (red line). (**b**) Microring modulation mechanism. The optical carrier is biased at the maximum slope of the microring transmission curve. When the RF frequency is equal to the free spectrum range (FSR) of the microring, the RF signal resonates in the loop together with the optical carrier to perform efficient electro-optical conversion.

The free spectrum range (FSR) of the LN waveguide microring resonator is also analyzed. FSR represents the distance between two adjacent resonance peaks, which can be expressed as:

$$f_{FSR} = \frac{\lambda^2}{L \cdot n_g}, \tag{1}$$

where L is the circumference of the microring, n_g is the group refractive index and λ is the optical carrier wavelength. For the radio frequency at 35 GHz, the calculated perimeter L = 3766.59 μm. In order to concentrate the electric field on the microring, special design is needed for the shape of the microring, as shown in Figure 1. It has several arcs with small bending radii and several straight lines. The bending loss of the structure is simulated, as shown in Figure 6. In order to show the influence of the bending radius R on the optical mode field distribution more intuitively, the logarithmic mode profile corresponding to R = 30 μm, 60 μm, 100 μm and straight waveguide is simulated. With the increasing of bending radius, the symmetry of the profile becomes better and closer to the case of straight waveguide. When the bending radius is greater than 100 μm, the loss tends to be flat and close to the straight waveguide loss. Therefore, the bending radius of 100 μm is finally selected.

As another important parameter of the microring, quality factor Q indicates the ability of the microring to store photons. As for a RF receiver, Q-factor can reflect the interaction between the carrier light wave and the incident RF electric field, where a high Q value means sharper resonance peaks, which can lead to longer lifetime of the photon in the ring and further generate strong interactions between the light field, enhancing the electric field, which ultimately make a higher sensitivity of the receiver. The value of Q can be expressed as:

$$Q = \frac{\pi n_g L}{\lambda} \frac{\sqrt{A(1-\kappa^2)}}{1 - A(1-\kappa^2)}, \tag{2}$$

where $A = \exp(-\alpha L)$ is the loss coefficient, α is the transmission loss of the waveguide and κ is the coupling coefficient. For the device design, the transmission loss is set to be 2.7 dB/m [24] which is the minimum loss value that can be achieved by the current processing technology, and the relationship between quality factor Q and coupling coefficient κ can

be analyzed, see Figure 7a. In the case of fixed gap, the length of coupling region L_{couple} is directly affected by the value of κ. As the coupling coefficient increased, Q showed a downward trend. To obtain a high-quality-factor, a smaller coupling coefficient should be selected, but this is at the cost of decreasing extinction ratio, as shown in Figure 7b. As the coupling coefficient is set to be κ = 0.08, the corresponding Q-factor is calculated to be around 10^6, and the coupling length L_{couple} = 0.7 μm.

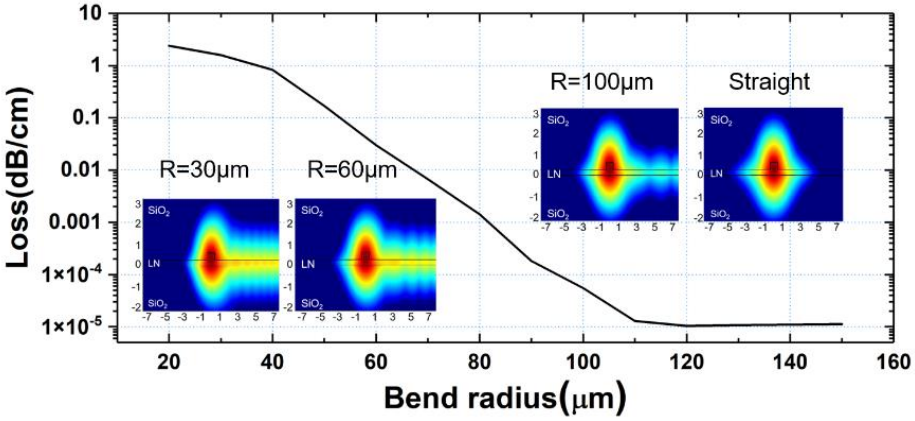

Figure 6. Relationship between the bend radius and optical loss. Simulations of the logarithmic mode profile corresponding to R = 30 μm, 60 μm, 100 μm and straight waveguide are reported in the insets.

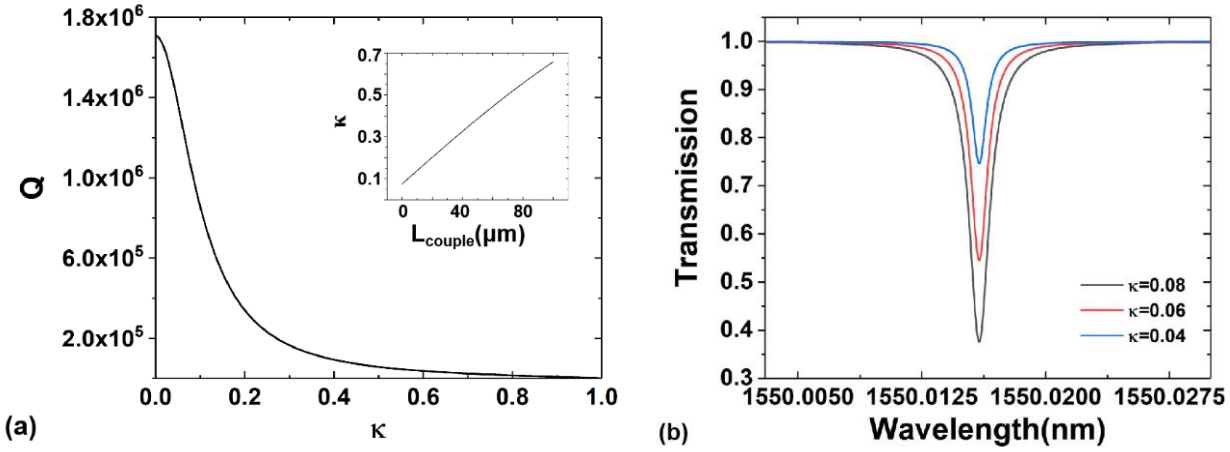

Figure 7. (**a**) Function relationship between quality factor (Q) and coupling coefficient κ. Inset: function of coupling coefficient κ and coupling length L_{couple} when gap = 0.8 μm. (**b**) Transmission line with coupling coefficient κ of 0.04, 0.06 and 0.08 around 1550 nm.

After the analysis and design mentioned above, the parameters of each part of the microring have been determined. It should be noted that when the modulated electric field is uniformly distributed on the microring, zero modulation phenomenon will occur [34], and the phase change of photons moving around in the ring is represented by [29]:

$$\Delta\varphi = -\frac{\pi n_{eff}^3 \gamma_{33} E_z L \Gamma}{\lambda}, \quad (3)$$

where E_z is the z-component of the electric with the direction perpendicular to the device surface, and Γ is the electro-optic overlap factor. Since $f_{FSR} = f_{RF}$, the time for the photon to travel a week in the ring is exactly equal to the time for the RF electric field to change for one cycle, resulting in zero phase change, as shown in Figure 8. In this work, a PPLN thin

film is introduced to have the left and right parts of the microring polarized with opposite directions, so that the maximum electro-optic modulation efficiency can be achieved. When a vertical electric field is applied to the surface of the chip, the modulated effective refractive index of the waveguide can be given by [35]:

$$n_{eff} = n_{eff0} - \frac{n_{eff0}^3 \gamma_{33} E_z \Gamma}{2}, \quad (4)$$

where n_{eff0} is the effective refractive index of waveguide without electric field. The simulation is performed using the following parameters: γ_{33} = 31 pm/V, n_{eff0} = 1.78596, Γ = 0.81. To observe the electro-optic effect, assuming that the applied electric field is uniform, the drift of the resonance peak near 1550 nm is investigated at different electric field intensities of 0 V/μm, 1 V/μm, 2 V/μm, 3 V/μm and 4 V/μm, respectively, as shown in Figure 9a,b, the electro-optical tunability of the RF receiver can be determined as 48 pm·μm/V, which is comparable to that of the structure with electrodes [36,37].

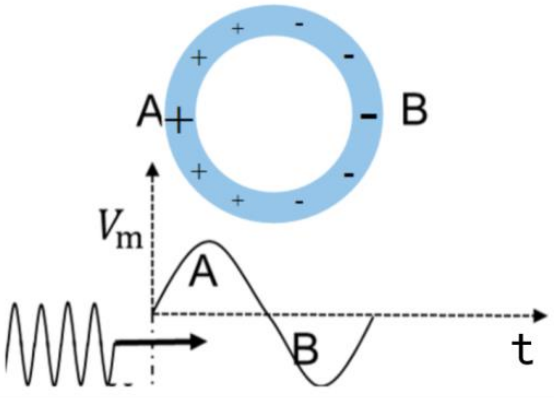

Figure 8. Zero modulation principle of uniform field. The blue area represents the microring, and the V_m-t curve below represents the change of electric field intensity over time. Since $f_{FSR} = f_{RF}$, the time for the photon to travel one cycle in the ring is exactly equal to the time for one period of RF electric field. When the uniform electric field acts on the microring and the photon is transmitted in region A of the microring, the RF electric field is positive, and the corresponding results in Equation (3) is Δφ. Similarly, as the photon travels through the B region of the microring, the RF electric field reverses and the corresponding phase change is −Δφ. As a result, the overall phase difference of photons around the microring is zero.

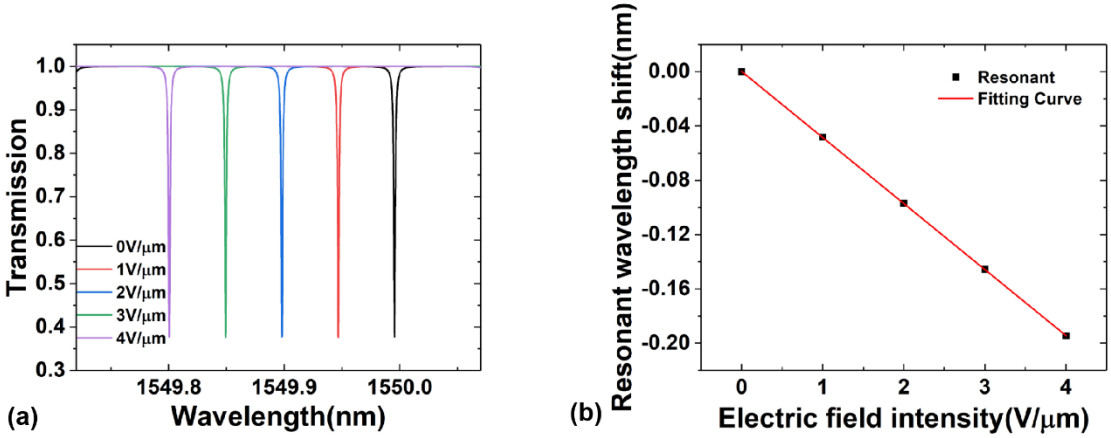

Figure 9. (**a**) The transmission spectrum and (**b**) wavelength offsets of the microring when the electric field intensity is 0 V/μm, 1 V/μm, 2 V/μm, 3 V/μm and 4 V/μm, respectively.

4. Conclusions

In conclusion, a microring-based electrode-free radio frequency receiver is designed using varFDTD and FDE solution methods, operating at 35 GHz RF electric field. Key parameters such as the coupling length of single-mode conditional transmission loss are analyzed and calculated. The Q-factor of the resonator is up to 10^6 and the total length of the ring is 3766.59 μm. PPLN technology is used to improve the electro-optic modulation efficiency, and the electro-optic tuneability reaches 48 pm·μm/V. This proposed device can be used with all dielectric antenna as a metal-free receiving front-end which will eliminate the weakness of traditional receivers and expect to play a key role in the field of anti-electromagnetic damage.

Author Contributions: Z.W. and M.Z. proposed the conceptualization and methodology; Z.W. analyzed the data, reviewed and modified the manuscript; Y.L. carried out the simulations, and wrote the paper; S.H., X.Y. (Xiong Yin) and M.D. contributed investigation; L.G. and X.Y. (Xin Yang) contributed data analysis and modification of the paper; M.Z. managed the project. All authors have read and agreed to the published version of the manuscript.

Funding: This work was supported by the Natural Science Foundation of China (NSFC) (61704017) and Dalian Science and Technology Innovation Fund (2018J11CY006).

Institutional Review Board Statement: The study was not applicable involving humans or animals.

Informed Consent Statement: The study was not applicable involving humans or animals.

Data Availability Statement: Data available in a publicly accessible repository.

Acknowledgments: Z. Wu, L. Guo and M. Zhao would like to acknowledge the support from the Natural Science Foundation of China (NSFC) (61704017) and Dalian Science and Technology Innovation Fund (2018J11CY006).

Conflicts of Interest: The authors declare no conflict of interest.

References

1. Rabiei, P.; Steier, W.H.; Zhang, C.; Dalton, L.R. Polymer micro-ring filters and modulators. *J. Light. Technol.* **2002**, *20*, 1968–1975. [CrossRef]
2. Hryniewicz, J.V.; Absil, P.P.; Little, B.E.; Wilson, R.A.; Ho, P.T. Higher order filter response in coupled microring resonators. *IEEE Photonics Technol. Lett.* **2000**, *12*, 320–322. [CrossRef]
3. Chen, L.; Reano, R.M. Compact electric field sensors based on indirect bonding of lithium niobate to silicon microrings. *Opt. Express* **2012**, *20*, 4032–4038. [CrossRef]
4. Huang, M.; Yang, J.; Jun, S.; Mu, S.; Lan, Y. Simulation and Analysis of a Metamaterial Sensor Based on a Microring Resonator. *Sensors* **2011**, *11*, 5886–5899. [CrossRef]
5. Zhou, L.; Sun, X.; Li, X.; Chen, J. Miniature Microring Resonator Sensor Based on a Hybrid Plasmonic Waveguide. *Sensors* **2011**, *11*, 6856–6867. [CrossRef]
6. Wan, L.; Chandrahalim, H.; Chen, C.; Chen, Q.S.; Mei, T.; Oki, Y.; Nishimura, N.; Guo, L.J.; Fan, X.D. On-chip, high-sensitivity temperature sensors based on dye-doped solid-state polymer microring lasers. *Appl. Phys. Lett.* **2017**, *111*, 061109. [CrossRef]
7. Tazawa, H.; Kuo, Y.H.; Dunayevskiy, I.; Luo, J.D.; Jen, A.K.Y.; Fetterman, H.R.; Steier, W.H. Ring resonator-based electrooptic polymer traveling-wave modulator. *J. Light. Technol.* **2006**, *24*, 3514–3519. [CrossRef]
8. Wang, C.; Zhang, M.; Stern, B.; Lipson, M.; Loncar, M. Nanophotonic lithium niobate electro-optic modulators. *Opt. Express* **2018**, *26*, 1547–1555. [CrossRef]
9. Chen, L.; Wood, M.G.; Reano, R.M. 12.5 pm/V hybrid silicon and lithium niobate optical microring resonator with integrated electrodes. *Opt. Express* **2013**, *21*, 27003–27010. [CrossRef]
10. Guarino, A.; Poberaj, G.; Rezzonico, D.; Degl'Innocenti, R.; Gunter, P. Electro-optically tunable microring resonators in lithium niobate. *Nat. Photonics* **2007**, *1*, 407–410. [CrossRef]
11. Zhang, M.; Buscaino, B.; Wang, C.; Shams-Ansari, A.; Reimer, C.; Zhu, R.R.; Kahn, J.M.; Loncar, M. Broadband electro-optic frequency comb generation in a lithium niobate microring resonator. *Nature* **2019**, *568*, 373–377. [CrossRef]
12. Stern, B.; Ji, X.C.; Okawachi, Y.; Gaeta, A.L.; Lipson, M. Battery-operated integrated frequency comb generator. *Nature* **2018**, *562*, 401–405. [CrossRef] [PubMed]
13. Bogaerts, W.; De Heyn, P.; Van Vaerenbergh, T.; De Vos, K.; Selvaraja, S.K.; Claes, T.; Dumon, P.; Bienstman, P.; Van Thourhout, D.; Baets, R. Silicon microring resonators. *Laser Photonics Rev.* **2012**, *6*, 47–73. [CrossRef]
14. Liu, M.; Yin, X.B.; Ulin-Avila, E.; Geng, B.S.; Zentgraf, T.; Ju, L.; Wang, F.; Zhang, X. A graphene-based broadband optical modulator. *Nature* **2011**, *474*, 64–67. [CrossRef] [PubMed]

15. Novoselov, K.S.; Fal'ko, V.I.; Colombo, L.; Gellert, P.R.; Schwab, M.G.; Kim, K. A roadmap for graphene. *Nature* **2012**, *490*, 192–200. [CrossRef] [PubMed]
16. Xu, Q.F.; Schmidt, B.; Pradhan, S.; Lipson, M. Micrometre-scale silicon electro-optic modulator. *Nature* **2005**, *435*, 325–327. [CrossRef] [PubMed]
17. Zhang, C.; Morton, P.A.; Khurgin, J.B.; Peters, J.D.; Bowers, J.E. Ultralinear heterogeneously integrated ring-assisted Mach-Zehnder interferometer modulator on silicon. *Optica* **2016**, *3*, 1483–1488. [CrossRef]
18. Timurdogan, E.; Sorace-Agaskar, C.M.; Sun, J.; Hosseini, E.S.; Biberman, A.; Watts, M.R. An ultralow power athermal silicon modulator. *Nat. Commun.* **2014**, *5*, 4008. [CrossRef] [PubMed]
19. Aoki, M.; Suzuki, M.; Sano, H.; Kawano, T.; Ido, T.; Taniwatari, T.; Uomi, K.; Takai, A. Ingaas/Ingaasp Mqw Electroabsorption Modulator Integrated with a dfb Laser Fabricated by Band-Gap Energy Control Selective-Area Mocvd. *IEEE J. Quantum Electron.* **1993**, *29*, 2088–2096. [CrossRef]
20. Lee, M.; Katz, H.E.; Erben, C.; Gill, D.M.; Gopalan, P.; Heber, J.D.; McGee, D.J. Broadband modulation of light by using an electro-optic polymer. *Science* **2002**, *298*, 1401–1403. [CrossRef] [PubMed]
21. Ahmed, A.N.R.; Shi, S.Y.; Zablocki, M.; Yao, P.; Prather, D.W. Tunable hybrid silicon nitride and thin-film lithium niobate electro-optic microresonator. *Opt. Lett.* **2019**, *44*, 618–621. [CrossRef]
22. Boes, A.; Corcoran, B.; Chang, L.; Bowers, J.; Mitchell, A. Status and Potential of Lithium Niobate on Insulator (LNOI) for Photonic Integrated Circuits. *Laser Photonics Rev.* **2018**, *12*, 1700256. [CrossRef]
23. Bahadori, M.; Yang, Y.S.; Goddard, L.L.; Gong, S.B. High performance fully etched isotropic microring resonators in thin-film lithium niobate on insulator platform. *Opt. Express* **2019**, *27*, 22025–22039. [CrossRef]
24. Zhang, M.; Wang, C.; Cheng, R.; Shams-Ansari, A.; Loncar, M. Monolithic ultra-high-Q lithium niobate microring resonator. *Optica* **2017**, *4*, 1536–1537. [CrossRef]
25. Cai, L.T.; Kong, R.R.; Wang, Y.W.; Hu, H. Channel waveguides and y-junctions in x-cut single-crystal lithium niobate thin film. *Opt. Express* **2015**, *23*, 29211–29221. [CrossRef]
26. Wang, Y.W.; Chen, Z.H.; Cai, L.T.; Jiang, Y.P.; Zhu, H.B.; Hu, H. Amorphous silicon-lithium niobate thin film strip-loaded waveguides. *Opt. Mater. Express* **2017**, *7*, 4018–4028. [CrossRef]
27. Jin, S.L.; Xu, L.T.; Zhang, H.H.; Li, Y.F. LiNbO3 Thin-Film Modulators Using Silicon Nitride Surface Ridge Waveguides. *IEEE Photonics Technol. Lett.* **2016**, *28*, 736–739. [CrossRef]
28. Wu, R.B.; Wang, M.; Xu, J.; Qi, J.; Chu, W.; Fang, Z.W.; Zhang, J.H.; Zhou, J.X.; Qiao, L.L.; Chai, Z.F.; et al. Long Low-Loss-Litium Niobate on Insulator Waveguides with Sub-Nanometer Surface Roughness. *Nanomaterials* **2018**, *8*, 910. [CrossRef]
29. Ayazi, A.; Hsu, R.C.J.; Houshmand, B.; Steier, W.H.; Jalali, B. All-dielectric photonic-assisted wireless receiver. *Opt. Express* **2008**, *16*, 1742–1747. [CrossRef] [PubMed]
30. Hsu, R.C.J.; Ayazi, A.; Houshmand, B.; Jalali, B. All-dielectric photonic-assisted radio front-end technology. *Nat. Photonics* **2007**, *1*, 535–538. [CrossRef]
31. Cohen, D.A.; Levi, A.F.J. Microphotonic components for a mm-wave receiver. *Solid·State Electron.* **2001**, *45*, 495–505. [CrossRef]
32. Schlarb, U.; Betzler, K. A generalized sellmeier equation for the refractive indices of lithium niobate. *Ferroelectrics* **1994**, *156*, 99–104. [CrossRef]
33. Jazbinsek, M.; Zgonik, M. Material tensor parameters of LiNbO3 relevant for electro- and elasto-optics. *Appl. Phys. B Lasers Opt.* **2002**, *74*, 407–414.
34. Ilchenko, V.S.; Savchenkov, A.A.; Matsko, A.B.; Maleki, L. Whispering-gallery-mode electro-optic modulator and photonic microwave receiver. *J. Opt. Soc. Am. B Opt. Phys.* **2003**, *20*, 333–342. [CrossRef]
35. Sun, Y.X.; Ji, W.; Yin, R.; Wu, C.H.; Gong, Z.S. The reconfigurable dispersion compensator based on LNOI waveguide grating. *Opt. Quantum Electron.* **2018**, *50*, 310. [CrossRef]
36. Han, H.P.; Xiang, B.X.; Zhang, J.L. Simulation and Analysis of Single-Mode Microring Resonators in Lithium Niobate Thin Films. *Crystals* **2018**, *8*, 342. [CrossRef]
37. Han, H.P.; Xiang, B.X. Simulation and analysis of electro-optic tunable microring resonators in silicon thin film on lithium niobate. *Sci. Rep.* **2019**, *9*, 6302. [CrossRef] [PubMed]